Journal of Materials Chemistry C

ROYAL SOCIETY OF CHEMISTRY

PAPER

View Article Online
View Journal

Cite this: DOI: 10.1039/d5tc04351d

Exploring lateral and vertical phase separation in SEBS and dibenzochrysene derivative polymer blends

Jiayi Chen, †[a] Piumi Kulatung, †[b] Félix Gagnon, [c] Surya Gayathri Bhattathiripad, [b] Jean-François Morin, *[c] Simon Rondeau-Gagné *[b] and Audrey Laventure *[a]

Received 11th December 2025,
Accepted 15th April 2026

DOI: 10.1039/d5tc04351d

rsc.li/materials-c

In this work, stretchable semiconducting blend films for organic field-effect transistors (OFETs) are prepared using a conjugated polymer derived from the vat dye Vat Orange 1 (VO1) and the thermoplastic elastomer SEBS. While the atomic force microscopy (AFM) images of the pristine films showed smooth, featureless morphologies for VO1 and the characteristic fibrillar texture for SEBS, blending the two materials resulted in a progressive increase in surface roughness. Additionally, as the VO1 content increased, distinct aggregate domains became apparent, suggesting partial phase separation within the composite films. X-ray photoelectron spectroscopy (XPS) depth profiling further confirmed a vertical phase separation, showing VO1 enrichment at both the dielectric interface and the film surface, while SEBS was predominantly localised in the middle of the film. Mechanically, the blended films sustained deformation exceeding 100%, a fivefold improvement over pristine VO1 films. This morphology ensures continuous semiconducting pathways for charge transport while imparting exceptional mechanical resilience. Organic field-effect transistors (OFETs) fabricated from VO1 : SEBS blends showed stable hole mobilities even at 10 wt% VO1 content, confirming preserved electronic connectivity despite significant dilution. The combination of intrinsic material stability, self-organized vertical morphology, and enhanced stretchability positions VO1 : SEBS composites as a promising platform for deformable, solution-processable organic electronics.

Introduction

In today's technology-driven era, progress in areas such as sustainable agriculture, personalized healthcare, next-generation communication systems, and renewable energy increasingly depends on the rational design of advanced materials tailored for specific functions and performance demands.[1–5] This strategy, which involves tailoring materials at the molecular or nanoscale level to meet specific functional needs, has already yielded transformative advancements from nanomaterials for targeted drug delivery[6] to light-harvesting materials in next-generation solar cells.[7,8] In the field of electronics, the rapid emergence of printed[9] and flexible electronics has been propelled by the rational design and synthesis of innovative materials.[10] This progress highlights the critical importance of achieving precise molecular-level control to unlock new technological capabilities. Among the most promising of these materials are organic semiconductors, particularly organic semiconducting polymers, which offer unique properties that enable the fabrication of soft, stretchable electronic devices.[11–13] Due to their extensive network of π-orbitals, these materials present favourable charge transport on par with those of amorphous silicon.[14–17] Moreover, they can be synthetically tailored with improved mechanical properties and unique features, including molecular self-healing or degradability, making them especially attractive for emerging fields such as bioelectronics and human-integrated systems.[18–20] These materials can be conformally integrated into everyday objects with complex geometries, facilitating applications in wearable technologies, smart packaging, and more.[21–23]

To achieve semiconducting polymer materials with improved mechanical and solid-state properties, a range of synthetic strategies have been developed. These strategies include the rational molecular engineering of side chains

[a] Département de Chimie, Université de Montréal, 1375 Avenue Thérèse-Lavoie-Roux, Montréal, QC, H2V 0B3, Canada. E-mail: audrey.laventure@umontreal.ca
[b] Department of Chemistry and Biochemistry, University of Windsor, 401 Sunset Avenue, Windsor, ON, N9B 3P4, Canada. E-mail: srondeau@uwindsor.ca
[c] Département de Chimie and CERMA, Université Laval, 1045 Avenue de la Médecine, Québec, QC, G1V0A6, Canada.
E-mail: Jean-Francois.Morin@chm.ulaval.ca
† J. C. and P. K. contributed equally to this work.

typically tailored to enhance solubility[24] and processability as well as modifications to the π-conjugated backbone,[10,18] which plays a central role in determining charge transport characteristics. Numerous semiconducting polymers designed with these strategies have demonstrated enhanced performance in various organic electronic applications. Another particularly effective approach involves the preparation of stretchable semiconducting composite materials.[9,25–27] This strategy is based on the physical blending of a rigid, semicrystalline semiconducting polymer with a soft, often elastomeric, material. The resulting polymer blends undergo phase separation, leading to the formation of discrete semiconducting domains within the elastomeric matrix. These domains promote molecular aggregation and ordering, facilitating efficient charge transport, while the elastomeric matrix imparts mechanical resilience, enabling the material to tolerate large strains without significant loss of electronic performance.

Over the years, numerous studies have demonstrated the effectiveness of this strategy. A notable example is the 2016 work by Reichmanis and coworkers, who that blending precured polydimethylsiloxane (PDMS) elastomer with poly(3-hexylthiophene) (P3HT) produced semiconducting composite films with significantly enhanced mechanical resilience under strain.[28] Remarkably, these composites also exhibited improved electrical performance in thin-film transistors (TFTs), with charge carrier mobilities reaching $\sim$0.18 $cm^2\ V^{-1}\ s^{-1}$, more than twice that of the P3HT PDMS-free control films. Another particularly influential example is the work by Bao and co-workers in 2017, in which they reported a stretchable semiconducting film composed of a high-mobility donor–acceptor diketopyrrolopyrrole-based (DPP) polymer blended with a low-modulus elastomer. The system exhibited strain tolerance up to 100% with minimal loss in field-effect mobility, attributed to the formation of interconnected semiconducting nanofibrils embedded in a continuous elastomeric network.[29] While numerous studies have established key design principles for achieving high-performance stretchable electronics particularly through controlled phase separation and network morphology,[30–32] research on semiconducting polymers has primarily focused on donor–acceptor (D–A) π-conjugated systems such as diketopyrrolopyrrole (DPP),[33–35] isoindigo,[36,37] and naphthalene diimide derivatives.[38–40] These materials have dominated the field due to their high charge carrier mobilities, tunable electronic properties, and strong intermolecular interactions.[41] However, these materials often suffer from inherent rigidity, high crystallinity, and limited solubility, which can constrain their processability and mechanical compliance. Efforts to blend these semiconductors with elastomers, such as PDMS or thermoplastic block copolymers,[30,31] have shown promise but also can result in non-ideal phase separation or compromised electronic performance due to the chemical incompatibility between the rigid π-conjugated backbone and the soft elastomeric matrix.

To further expand the toolkit of semiconducting polymer composites and explore new systems that could lead to combined processability, improved charge transport and high mechanical resilience, herein we report the preparation of VO1-based semiconducting polymers with polystyrene-*block*-poly(ethylene-*ran*-butylene)-*block*-polystyrene (SEBS) and the characterization of their solid-state, electronic and mechanical properties in thin films and TFT devices. VO1 pigment-based semiconducting polymers offer a compelling alternative to poly(thiophene) and rigid D–A polymer systems. Derived from industrial dye precursors, these materials feature extended conjugation, high thermal and photochemical stability, and intrinsic planarity that promotes π-stacking.[35,40,42] Unlike many traditional D–A polymers, previous works by us and others demonstrated that VO1-based systems can possess lower crystallinity and reduced backbone stiffness,[43] enabling greater compatibility with flexible substrates and mechanical blending approaches. Furthermore, their robust chemical structure and favorable redox properties make them attractive candidates for stable, high-performance organic electronics. To harness the potential of VO1 pigment-based semiconductors, we blended them with a compatible elastomer. SEBS was selected as an ideal matrix due to its excellent stretchability,[44] chemical resistance, and processability. Its nanostructured morphology also enables controlled phase separation, supporting improved mechanical properties and charge transport.[34,45] Using a multimodal characterization approach, combining atomic force microscopy (AFM), X-ray photoelectron spectroscopy (XPS) and X-ray scattering, we meticulously prepared various composites by systematically varying blend ratios between the VO1 dye-based polymer, and the SEBS. Our results confirmed that the addition of SEBS to VO1 can significantly impact lateral phase separation and nanoscale structures. Additionally, the polymer blends showed interesting vertical phase separation that also shown significant impact on the mechanical and electronic properties of the new materials. By exploring the blending of VO1 pigment-based semiconducting polymers with SEBS, this work develops composite materials that combine the intrinsic stability and tunable optoelectronic properties of VO1 systems with the mechanical robustness and stretchability of elastomers. This approach offers a promising pathway toward deformable, solution-processable, and scalable semiconducting materials for next-generation flexible and wearable electronics.

Experimental section

Materials

Commercial reagents were used without further purification unless otherwise specified. SEBS (H1052) was purchased from Asahi Kasei, and the VO1 polymer was synthesized following a previously reported procedure with a M_n = 17.4 kg mol^{-1}.[43] In this work, we used the polymer referred to as **P2** in the original publication, whose structure is presented in Scheme 1. For clarity, the Vat Orange 1 based polymer **P2** will hereafter be referred to as VO1.

Polymer blend and spin-coated films preparation

Spin-coated films of SEBS, VO1 and their blends were prepared by dissolving each polymer in separate vial in chlorobenzene at

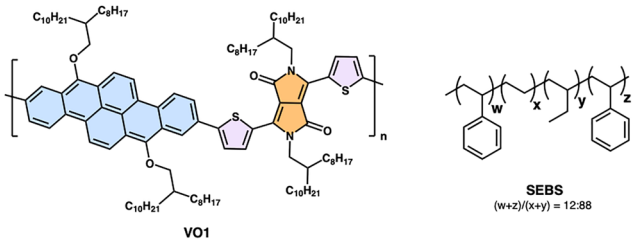

Scheme 1 Molecular structure of VO1 and SEBS.

10 mg mL^{-1} and stirred overnight at room temperature. The blends are prepared by mixing the appropriate weight ratio of each polymer solution (ex: 50 : 50 VO1 : SEBS corresponds to mixing 2 mL of a 10 mg mL^{-1} VO1 solution and 2 mL of a 10 mg mL^{-1} SEBS solution). The spin-coating parameters are 1500 rpm for 60 s.

UV-vis

Transmission UV-vis measurements were performed using a Cary 60 spectrophotometer on both solutions and drop-cast films. In both cases, chloroform was used as the solvent and it was chosen to facilitate solvent evaporation during film formation.

Thermal properties

Thermogravimetric analysis was performed using a TGA Q600 (TA Instruments) from 30 °C to 500 °C under a nitrogen atmosphere at a heating rate of 10 °C min^{-1}. Differential scanning calorimetry (DSC) analyses were performed using a DSC Q1000 (TA Instruments) from −60 to 300 °C with a heating and cooling rate of 10 °C min^{-1} under a nitrogen atmosphere. The first heating run was performed to erase the thermal history of the samples, followed by cooling and a second heating run to determine the transition temperatures of the compounds. A calibration using indium was run before the measurements.

Atomic force microscopy

The morphology of polymer blends was assessed using a multimode atomic force microscope (AFM, Digital Instruments) operated in the tapping mode at room temperature. AFM images were collected using Nanoscope 6 software and processed using Nanoscope analysis software, they were recorded on spin-coated samples using a Dimension ICON microscope with Nanoscope V controller (Bruker, Santa Barbara, CA, USA). All images were acquired using tapping mode and were performed at a scanning rate of 1 Hz. A probe (model: TESPA) with a 125 μm microlever of length having a spring constant of 42 Newton m^{-1} and a tip of <8 nm radius was used. At the time of acquisition, the resonant frequency of the microlever was around 320 kHz. All surfaces were imaged using oscillation damping between 15–20%. Nanomechanical imaging was performed using a RTESPA-300-30 pre-calibrated tips. The scan resolution was set to 256 lines. The thickness of the samples is determined by scanning an area that has been scratched by a tweezer.

X-ray photoelectron spectroscopy (XPS)

XPS was performed on spin-coated samples using an VG Escalab 250Xi (Thermo Fisher Scientific) with a monochromated Al K_α source at a power of 218.8 W (14.7 kV, 14.9 mA) and a 180° spherical sector analyzer with constant analyzer energy transmission mode. Standard charge compensation using low energy electrons and Ar^+ ions was used. The pressure in the analysis chamber during analysis was around 1.0×10^{-8} Torr. Survey spectra were acquired at a pass energy of 200 eV and a step size of 1 eV. High-resolution spectra were acquired for silicium (Si 2p), sulfur (S 2s), oxygen (O 1s), carbon (C 1s) and nitrogen (N 1s) at 200 eV pass energy and step size 0.5 eV. Specimens were analyzed at an emission angle of 0° with respect to surface normal. Data processing was performed using Avantage v6.5.0 (Thermo Fisher Scientific). The atomic concentrations were calculated using integral peak intensities and the sensitivity factors supplied by the manufacturer. Binding energies were referenced to the C 1s peak at 285.0 eV for aliphatic hydrocarbons.

Grazing-incidence wide-angle X-ray scattering (GIWAXS)

GIWAXS was performed on beamline BL13A with a wavelength of 1.02042 Å (12 kev) at the Taiwan Light Source (TLS) of National Synchrotron Radiation Research Center (NSRRC). All the measurements of the transistors were conducted using a Keithley 4200 semiconductor parameter analyzer (Keithley Instruments Inc., Cleveland, OH, USA) under dry N_2 (glovebox) and at room temperature.

Crack onset strain measurement

The polymer blend solutions were spin-coated on poly(sodium 4-styrenesulfonate) (PSS, M_w = 70 kg mol^{-1}, powder) coated glass slides prepared by spin-coating (700 rpm for 30 s) a 50 mg mL^{-1} aqueous solution of PSS in water. Polydimethylsiloxane (PDMS) was used as the elastomer substrate mixed at a base-to-crosslinker ratio of 15 : 1 and cross-linked at 70 °C overnight. PDMS strips were placed on the coated PSS glass slide with polymer blend and then immersed in water for 10 min. Consequently, the PSS layer was dissolved, and a thin film was attached to the PDMS. Then, PDMS was stretched to the selected strain elongation using a microscope stretcher. In the final step, the stretched-thin films were transferred onto the Si wafers and characterized using optical microscopy.

Device fabrication

Organic field-effect transistors (OFET) devices were fabricated on highly doped n-type Si(100) wafers with 300 nm thick SiO_2 functionalized with an *n*-octadecyltrimethoxysilane (OTS) self-assembled monolayer, according to reported methods.[46] The OTS-treated substrate was washed with toluene, acetone, and isopropanol, and then dried with nitrogen before use. Next, polymer solutions were spin-coated on OTS-coated Si wafers at 2000 rpm for 1 min. As-cast and annealed (100 °C for 30 min)

films were prepared. Source and drain top electrodes were then deposited by evaporating gold (50 nm) through a shadow mask with a channel length (L) and width (W) defined as 100 and 1000 μm, respectively. A shadow mask with a channel length (L) and width (W) defined as 100 and 1000 μm, respectively, was used for stretched devices. All measurements were conducted using a Keithley 4200-SCS semiconductor parameter analyzer (Keithley Instruments Inc., Cleveland, OH, USA) in an N_2-filled glove box at room temperature.

Transfer-printed organic field-effect transistor (OFET) fabrication

To measure the charge mobilities upon stretching, a lamination procedure adapted from previous literature was used to laminate the semiconducting polymer films onto PDMS.[47,48] The resulting thin films supported on PDMS were stretched to 25% strain and laminated back to Si wafers. Source and drain top electrodes were deposited parallel and perpendicular to the stretching direction by evaporating gold (50 nm) through a shadow mask with a channel length (L) and width (W) defined as 100 and 1000 μm, respectively. All measurements were conducted using a Keithley 4200-SCS semiconductor parameter analyzer (Keithley Instruments Inc., Cleveland, OH, USA) in an N_2-filled glove box at room temperature.

Results and discussion

Building on previous studies, we selected a copolymer of 2,9-dibromo-dibenzo[*b*,*def*]chrysene-7,14-dione (Vat Orange 1, VO1) and diketopyrrolopyrrole (DPP) for this work with its RMN and GPC in the Fig. S1 and S2 respectively.[43] Owing to its favorable charge-transport properties and its predominantly amorphous nature, two attributes that facilitate polymer blending and enhance mechanical compliance. To enhance the mechanical robustness of the resulting films, SEBS H1052 was incorporated at various weight ratios. The molecular structures of both compounds are shown in Scheme 1. This grade of SEBS was chosen for its high midblock content and optimized molecular weight, offering a well-balanced combination of elasticity and mechanical strength. Its low hardness and high elongation at break make it ideal for flexible electronics, while its thermoplastic processability ensures compatibility with solution-based fabrication. The VO1 polymer was synthesized according to a previously reported method,[43] and complete experimental details on blend and film preparation are provided in the Experimental section.

Nanoscale morphology of VO1 : SEBS polymer blends in thin films

Understanding the morphology of polymer blends is crucial to investigate and control their properties in devices. Particularly important is the nanoscale roughness and phase separation, which are key parameters influencing optoelectronic and thermomechanical properties.[49–51] First, the solid-state morphology of VO1 : SEBS blends in thin films was investigated using atomic force microscopy (AFM) to get insights on how the addition of VO1 affects the structural organization of both polymers. The results are depicted in Fig. 1 and Table S2. All films showed comparable thickness, found to range between 35 to 43 nm. Films prepared from pure VO1 polymer (Fig. 1a)

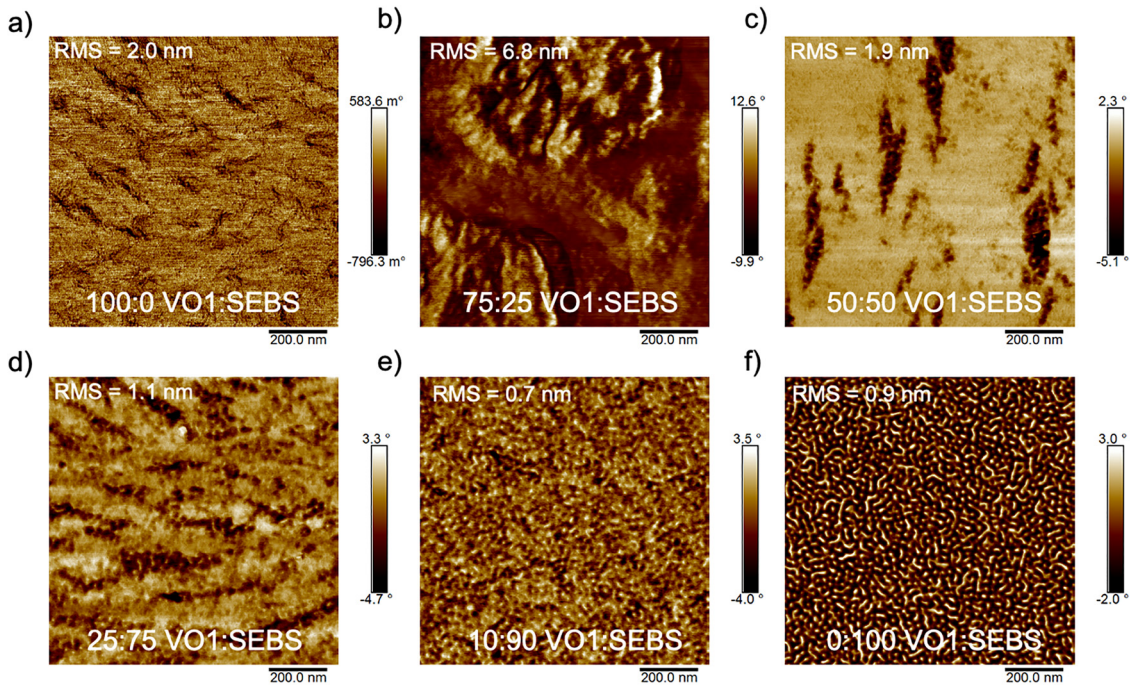

Fig. 1 Atomic force microscopy (AFM) phase images of VO1 : SEBS spin-coated films of (a) 100 : 0 VO1 : SEBS, (b) 75 : 25 VO1 : SEBS, (c) 50 : 50 VO1 : SEBS, (d) 25 : 75 VO1 : SEBS, (e) 10 : 90 VO1 : SEBS, (f) 0 : 100 VO1 : SEBS.

showed a uniform film morphology without well-defined domains. This observation is supported by differential scanning calorimetry (DSC), which shows no detectable thermal transitions (Fig. S3), and by UV-visible spectroscopy, where the film spectrum appears as a broadened version of the solution spectrum (Fig. S4) strongly indicating that the VO1 polymer remains amorphous in the solid state. Additionally, AFM reveals that the surface roughness of the VO1 film is approximately twice that of neat, fibrillar SEBS, with a root-mean-square (RMS) roughness of 2.0 nm. In contrast, pure SEBS film (Fig. 1f) showed a typical fibrillar structure and a low surface RMS roughness value of 0.9 nm (Table S2). As the SEBS content is progressively increased (from 75 : 25 to 10 : 90 VO1 : SEBS), the VO1 polymer becomes increasingly distributed throughout the film, the formation of interpenetrated domains suggests that the blend lies within the spinodal region of the phase diagram, corresponding to a thermodynamically unstable state. Notably, fibrillar features of SEBS are still visible within the blends, potentially indicating that the VO1 polymer predominantly resides above the SEBS matrix. This observation suggests a potential vertical phase separation between the two components, with VO1 preferentially locating near the film surface. At high VO1 loading (75 : 25 VO1 : SEBS), a distinct morphological transition is observed: the discrete VO1-rich droplets observed at 75 : 25 VO1 : SEBS indicate that the system has entered a metastable region[52] of the phase diagram. In this regime, the lack of connectivity between VO1 domains, unlike an interpenetrated network,[26] may hinder efficient charge transport and thus negatively impact charge mobility. This phenomenon leads to a notable increase in surface roughness to 6.8 nm, clearly evidenced in the AFM height images (Fig. S5), particularly in the 10 × 10 μm topography scan (Fig. S5b). Overall, despite observing signs of vertical phase separation, all films showed relatively smooth surface morphology, with RMS roughness ranging from 6.8 to 0.7 nm for 75 : 25 and 10 : 90 VO1 : SEBS respectively. Height images follow the same overall trend as the phase images, reinforcing the presence of vertical phase separation. Phase separation primarily depends on the molecular structure, molecular weight, and blend ratio.[53] Since all our VO1 : SEBS blends exhibit vertical phase separation, this behavior is likely governed by differences in molecular structure and molecular weight, which in turn lead to variations in surface energy.[53,54]

To further investigate and confirm the potential vertical phase separation observed in the AFM phase images, X-ray photoelectron spectroscopy (XPS) was performed, and the results are depicted in Fig. 2. Notably, while AFM provides valuable insights into the surface morphology and lateral distribution of the polymers, XPS can allow for a more detailed investigation of the vertical arrangement by tracking the atomic composition throughout the film. In this work, we specifically used sulfur content, which is specific to VO1, as a reliable marker to distinguish VO1 from SEBS and assess its distribution across different blend ratios. The silicon atomic percentage was used as a reference marker for the film thickness; plateauing of the silicon atomic percentage was correlated to the end of the VO1 : SEBS film and marked the final etching time. It is important to note that the time to reach out this plateauing of the Si signal decreased with increasing VO1 content dropping from approximately 310 s for 0 : 100 VO1 : SEBS (Fig. 2f) to 250 s for 100 : 0 VO1 : SEBS (Fig. 2a). This reflected a relative ease of removing VO1 under ion bombardment, potential attributed to soft mechanical nature of the semiconducting polymers making it more susceptible to sputtering compared to the more rigid and phase-separated morphology of SEBS. As expected, the sulfur content in pristine SEBS (Fig. 2f) remained at 0% throughout the entire profile, while the atomic percentage of carbon remained close to 100%

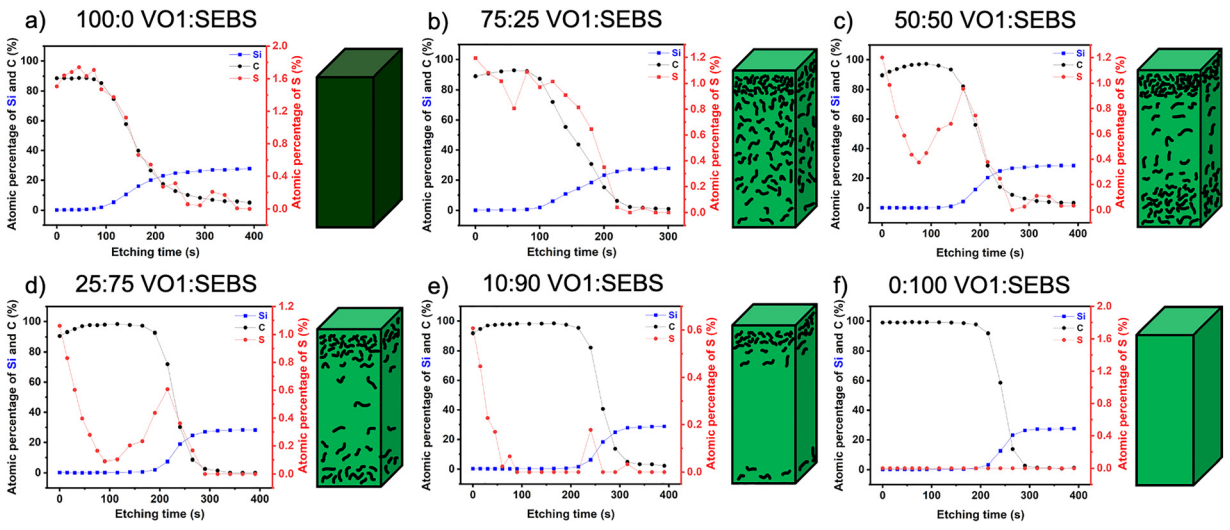

Fig. 2 X-ray photoelectron spectroscopy (XPS) atomic percentage profiles of Si, C and S as a function of etching time for VO1 : SEBS spin-coated films: (a) 100 : 0 VO1 : SEBS, (b) 75 : 25 VO1 : SEBS, (c) 50 : 50 VO1 : SEBS, (d) 25 : 75 VO1 : SEBS, (e) 10 : 90 VO1 : SEBS, and (f) 0 : 100 VO1 : SEBS. Each green rectangular prism represents the SEBS matrix, while the black worm-like structures within the prisms illustrate the distribution of the VO1 polymer, highlighting the vertical phase separation at different ratios.

until the substrate was reached. In contrast, the pristine VO1 sample (Fig. 2a) showed parallel depth trends for carbon and sulfur, both decreasing steadily as etching progresses toward the silicon substrate, consistent with uniform composition throughout the film. For the VO1 : SEBS blends, carbon trends mirror those observed in the pristine films. However, trends in sulfur percentages showed a non-monotonic profile for all blends. In all cases, S percentages were found to be at their highest at the film surface (0 s). Upon sputtering, a decreased to a local minimum near the film's midpoint was observed, followed by an increase again toward a second local maximum near the substrate interface before finally dropping as the silicon substrate is reached. This overall behaviour, observed in all blends, was directly correlated to a vertical phase separation, with sulfur-rich VO1 concentrated at both interfaces and depleted in the center. Notably, the effect becomes more pronounced with decreasing VO1 content. In the 10 : 90 VO1 : SEBS blend (Fig. 2e), sulfur becomes nearly undetectable at the film's center, indicating a strong vertical segregation where the VO1 component is largely excluded from the mid-film region due to incompatibility with SEBS. Overall, these results confirm that the VO1 polymer domains are mainly located at the top and bottom of the film, which agrees with the VO1 : SEBS vertical phase separation observed in the AFM images. This phenomenon is particularly compelling in OFETs, as vertical phase separation can potentially offer a strategy to decouple mechanical and electronic functions within a single active layer. This self-organized vertical stratification also can hold promise for large-scale manufacturing by enabling desirable solid-state morphology through single-layer deposition, thus reducing the need for complex multi-layer coating steps.

The influence of SEBS on the thin-film morphology of the polymer blends was also investigated using grazing incidence wide-angle X-ray scattering (GIWAXS). Fig. S6 presents both 2D and integrated 1D scattering patterns for all blend compositions, while Table S1 summarizes the extracted *d*-spacing values. Across all samples, the absence of well-defined diffraction peaks was observed, confirming that the blends are predominantly amorphous, independently of the blend ratio. A weak (100) diffraction peak was observed only for the pristine VO1 polymer and the 75 : 25 VO1 : SEBS blend. For the pristine polymer, this peak appears in the out-of-plane direction at q_z = 0.332 Å^{-1}, corresponding to a *d*-spacing of ~18.9 Å. Upon incorporation of SEBS (up to 25%), the *d*-spacing increased to ~23.0 Å. (q_z = 0.273 Å^{-1}), indicating disruption of molecular packing with increasing SEBS content. This observation is consistent with previous literature reports.[27,55]

Impact of blending on the mechanical properties in thin films

Following the characterization of the nanoscale structure of the polymer blends in thin films, the mechanical behavior of the VO1 : SEBS blend in thin films was characterized to assess their suitability for flexible electronics. To this end, crack onset strain measurements were performed using pseudo-free-standing film tensile pull testing on samples laminated onto elastomeric substrates, following previously established protocols.[47,56] The detailed experimental procedure is provided in the experimental section, and the results are summarized in Fig. 3 (all the results can be found in SI in Fig. S7). Briefly, thin films were first laminated onto PDMS substrates, subjected to uniaxial stretching across a strain range of 0–100%, and then transferred back onto glass slides for characterization by optical microscopy. As shown in Fig. 3b, the pristine VO1-based

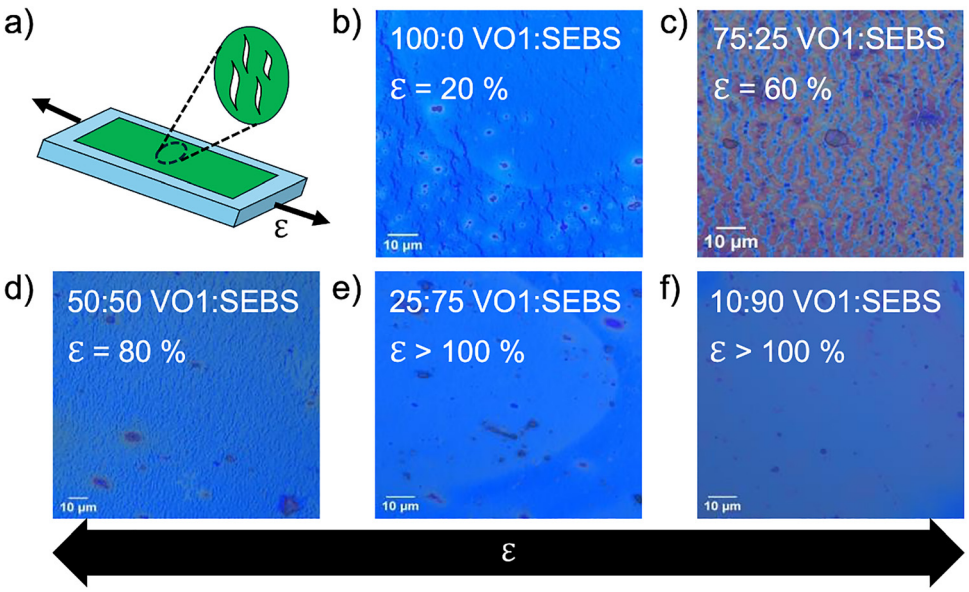

Fig. 3 Impact of the blending ratio on crack onset strain. (a) Scheme of the stretching during the crack onset strain test where the white features corresponds to cracks. Optical microscopy images of stretched thin films: (b) 100 : 0 VO1 : SEBS, (c) 75 : 25 VO1 : SEBS, (d) 50 : 50 VO1 : SEBS, (e) 25 : 75 VO1 : SEBS, (f) 0 : 100 VO1 : SEBS at up to 100% strain elongation.

polymer film exhibited limited stretchability, with cracks initiating at strain levels as low as ~20%. In contrast, the incorporation of SEBS led to a significant improvement in mechanical compliance. For blends containing 75 : 25 and 50 : 50 VO1 : SEBS, the crack onset strain increased to ~60% and ~80%, respectively. At higher SEBS loadings (25 : 75 and 10 : 90 VO1 : SEBS), the films tolerated up to 100% strain without visible cracking. This substantial enhancement in mechanical robustness is attributed to the elastomeric nature of SEBS, which acts as a flexible matrix that absorbs strain and inhibits crack propagation. Similar behavior has been reported in blends of SEBS with DPP-based semiconducting polymers, where nanofibrous networks of the conjugated polymer are embedded within the elastomeric matrix, maintaining charge transport while enhancing mechanical deformability.[57,58] In the present system, a comparable interaction is likely, where SEBS distributes stress and suppresses mechanical failure within the film. It is important to acknowledge, however, that crack onset strain is influenced by several factors beyond blend composition, including film uniformity, interfacial adhesion, and the presence of defects introduced during film preparation or transfer.[34,59]

To gain deeper insights into the mechanical behavior of the blended films, quantitative nanomechanical mapping (QNM) was performed using AFM. Representative nanomechanical images of VO1 : SEBS blend films at 100 : 0, 50 : 50, and 10 : 90 VO1 : SEBS are shown in SI in Fig. S8, while corresponding force–distance curves are provided in Fig. S9. To ensure reliable and representative modulus values, measurements were conducted at ten different locations per sample, and the averaged results are reported. The measurements were carried out using a soft cantilever in intermittent contact mode under a constant force setpoint, enabling the acquisition of force–distance spectra that were converted into quantitative nanomechanical property maps.[7] These maps help visualize both surface-dominated properties (adhesion and dissipation) and subsurface mechanical properties (modulus and deformation). Focusing first on modulus, derived from the Derjaguin–Müller–Toporov (DMT) model, this parameter quantifies material stiffness. Pristine VO1 films exhibited a high modulus of 7.4 GPa, indicative of their rigid nature. With increasing SEBS content, the modulus dropped significantly, decreasing to 5.8 GPa in the 50 : 50 VO1 : SEBS blend and further to 1.4 GPa at 10 : 90 VO1 : SEBS. This demonstrates a clear softening of the film upon addition of SEBS, as expected. These values correlate well with crack-onset strain measurements and confirm that SEBS incorporation imparts increased elasticity and stretchability. Notably, the deformation maps reinforce this trend. In these images, higher deformation, typically corresponding to softer regions, is shown in lighter colors. The 100 : 0 VO1 : SEBS film primarily displayed low-deformation (darker red) regions, while increasing SEBS content introduced more extensive high-deformation areas, especially in the 10 : 90 VO1 : SEBS blend. This inverse relationship between modulus and deformation is consistent across all compositions, with softer domains showing greater elastic response under load. Surface energy dissipation, which reflects viscoelasticity and energy loss during tip, sample interaction, also changed markedly with composition. In pristine VO1 films, dissipation maps predominantly exhibited green and blue tones, indicating minimal energy loss associated with the stiff, ordered polymer. With the addition of SEBS (50 : 50 and 10 : 90 VO1 : SEBS), orange-toned regions became increasingly visible, reflecting enhanced viscoelasticity and energy dissipation characteristic of the elastomeric SEBS phase. Adhesion maps, which capture the force required to detach the AFM tip from the surface, revealed additional compositional effects. The 100 : 0 VO1 : SEBS film showed predominantly dark blue areas, indicative of low surface adhesion, likely due to its less deformable and chemically inert surface. In contrast, blends of 50 : 50 and 10 : 90 VO1 : SEBS exhibited lighter blue regions, consistent with increased adhesion. This rise in adhesion is attributed to enhanced tip–surface interaction in the softer, more compliant SEBS-rich regions.

Overall, results from QNM analysis revealed substantial changes in both surface and subsurface mechanical properties with increasing SEBS content. The observed reductions in modulus, increases in deformation, dissipation, and adhesion collectively highlight the elastomeric character of SEBS and its key role in improving mechanical flexibility and durability of the VO1-based blend films. These findings support earlier observations from crack-onset strain testing and further validate the mechanical advantages of incorporating SEBS into semiconducting polymer matrices for stretchable electronics.

Impact of blending ratios on the electronic properties in OFETs

Having established the strong correlation between blend composition and mechanical flexibility, the next step was to examine how these morphological and mechanical changes influence the electrical performance of the VO1 : SEBS-based OFETs. This characterization was performed to get insights into the impact of the addition of the insulating SEBS on the charge transport of the semiconducting polymers. The key device parameters, including hole mobility, threshold voltage, and on/off ratios, are summarized in Table 1 and corresponding transfer and output curves are presented in the Fig. S10 and S11, and transfer curves of different VO1 : SEBS ratio before thermal annealing are summarized in the Fig. S12. Across all blend compositions, OFET devices exhibited modest on/off ratios (~10^2), consistent with the predominately amorphous nature of the VO1 polymer and the absence of strong long-range order.

However, both blend ratio and annealing treatment significantly influenced charge carrier mobility and threshold voltages. As-cast films generally showed slightly higher or comparable hole mobilities than their annealed counterparts, suggesting that low-temperature thermal treatment may not significantly enhance π–π stacking or film ordering in these predominantly amorphous systems. Notably, the 75 : 25 VO1 : SEBS blend exhibited the highest average and maximum hole mobility among all samples (μ_h^{ave} = 5.30 × 10^{-5} cm^2 V^{-1} s^{-1}), outperforming even the pristine 100 : 0 VO1 : SEBS film. Interestingly, the 10 : 90 VO1 : SEBS devices also showed relatively

Table 1 Electronic properties of the polymer blends in organic field-effect transistor (OFET) devices. Average (μ_h^{avg}) and maximum hole mobilities (μ_h^{max}), threshold voltages (V_{th}), and I_{on}/I_{off} ratios for OFETs fabricated using polymer blends (100 : 0 to 10 : 90 VO1 : SEBS) before and after thermal annealing. The device performances were averaged from 10 devices and *W*/*L* represents the width/length channel ratio

Blend ratio VO1 : SEBS	Annealing temperature (°C)	*W*/*L*	μ_h^{avg}/μ_h^{max} ($cm^2\ V^{-1}\ s^{-1}$) × 10^{-5}	I_{on}/I_{off}	V_{th}^{avg} (V)
100 : 0	As cast	10	4.8 ± 0.5/5.5	10^2	−26.3 ± 1.8
	100		4.0 ± 0.4/4.4		−34.0 ± 4.0
75 : 25	As cast	10	5.3 ± 0.7/6.6	10^2	−25.9 ± 1.6
	100		4.8 ± 0.8/5.8		−33.8 ± 3.0
50 : 50	As cast	10	5.0 ± 0.6/5.7	10^2	−30.7 ± 2.6
	100		4.8 ± 0.4/5.2		−37.9 ± 4.4
25 : 75	As cast	10	3.2 ± 0.3/3.6	10^2	−35.0 ± 1.0
	100		3.1 ± 0.4/3.7		−36.8 ± 5.2
10 : 90	As cast	10	5.3 ± 0.1/7.2	10^2	−18.4 ± 2.8
	100		3.6 ± 0.1/5.0		−36.0 ± 3.8

comparable as-cast mobility (7.21×10^{-5} $cm^2\ V^{-1}\ s^{-1}$), which could result from percolative pathways forming at low VO1 loadings due to vertical segregation. Thermal annealing consistently induces a negative shift in threshold voltage across all samples, with shifts as large as ~10 V observed. The threshold voltage (V_{th}) is comparatively high for this blend, possibly due to a thinner or more discontinuous semiconducting layer at the dielectric interface, consistent with sulfur depletion observed in XPS depth profiling. Beyond the observed trends, the relative stability of charge transport properties upon blending with SEBS highlights the beneficial impact of vertical phase separation. As the SEBS content increases, the elastomer tends to segregate toward the middle of the film, leaving a relatively undisturbed semiconducting layer at the dielectric interface, where charge transport predominantly occurs in OFETs. This vertical stratification, combined with only moderate lateral phase separation, minimizes disruption to the percolative pathways of the semiconducting polymer. As a result, key device parameters such as mobility (Fig. 4a) and threshold voltage (Table 1) remain largely preserved despite the reduction in the film modulus (Fig. 4b). Beyond thermal annealing, the next step is to examine the effect of mechanical deformation on the device performance.

Performance of VO1 : SEBS-based OFET devices upon mechanical deformation

To assess the electronic performance of VO1 : SEBS polymer blends, a 25 : 75 VO1 : SEBS blend, chosen based on its favorable crack-onset strain, was subjected to mechanical elongation up to 50% strain, a value exceeding the typical elongation range of human skin (25–30%).[60] Electrical measurements were performed post-stretching, and the results are summarized in Fig. S13 and Table S3. Despite the substantial deformation experienced at 25% strain elongation, the devices retained characteristic OFET behavior, including well-defined transfer and output curves (Fig. S14 and S13). While a modest reduction in mobility was observed under strain, values remained within the same order of magnitude. Interestingly, upon further stretching from 25% to 50%, a slight increase in mobility was recorded. This improvement, consistent across both parallel and perpendicular orientations, suggests strain-induced alignment or densification of semiconducting domains, a phenomenon previously observed in other conjugated polymer systems.[61] The observed mechanical and electrical stability under strain highlights the role of SEBS in dissipating mechanical stress while maintaining the structural and functional integrity of the semiconducting network. By acting as a compliant, strain-absorbing matrix, SEBS enables the blend films to deform

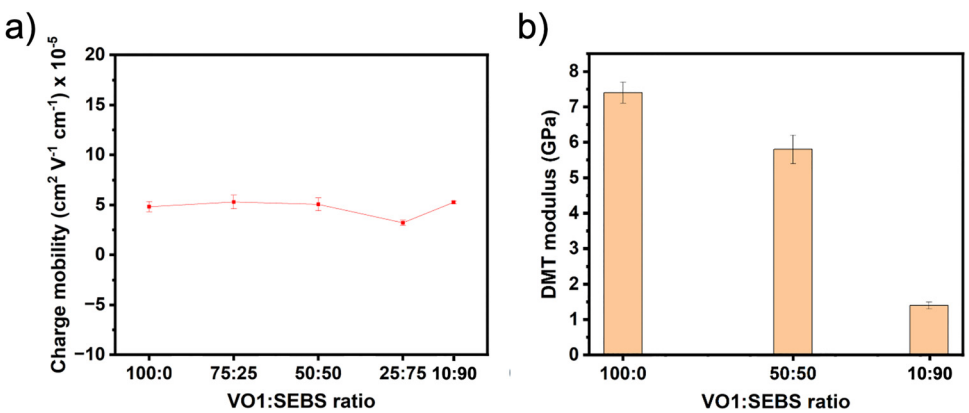

Fig. 4 (a) Average charge carrier mobility of different polymer blends for thin films as-cast and (b) corresponding Derjaguin–Müller–Toporov (DMT) moduli of the various VO1 : SEBS blends evaluated using quantitative nanomechanical mapping (QNM).

without interrupting the charge transport pathways established by the VO1 domains.

Conclusion

In summary, this study demonstrates the development of stretchable semiconducting blend films composed of a VO1 pigment-derived conjugated polymer and SEBS. Through a comprehensive investigation of morphology, mechanical response, and electronic properties, we showed that blending with SEBS enables significant mechanical compliance while preserving charge transport characteristics, an essential requirement for next-generation flexible and wearable electronics. The predominantly amorphous nature of the VO1 polymer was confirmed through optical spectroscopy and X-ray scattering, with no detectable crystalline peaks and broad absorption features consistent with disordered π–π stacking. QNM analysis (AFM) revealed that the elastic modulus of the pristine VO1 film was decreased upon blending, highlighting the progressive softening of the film with increasing SEBS content. Notably, XPS depth profiling and AFM phase imaging showed strong evidence of vertical phase separation, where the semiconducting VO1 polymer localised at the dielectric interface, while SEBS segregated toward the middle and upper regions of the film. This morphology was maintained even at low VO1 concentrations, enabling continuous semiconducting pathways at the interface where charge transport occurs in OFETs. OFET devices fabricated in a bottom-gate, top-contact configuration using these blends displayed consistent performance across compositions. Pristine VO1 devices exhibited an average hole mobility of 4.8×10^{-5} cm^2 V^{-1} s^{-1}, and this value remained largely unchanged across blends with 75 : 25, 50 : 50, and even 10 : 90 VO1 : SEBS, demonstrating that charge mobility was unaffected by dilution with SEBS due to the maintained percolation network at the interface. Finally, mechanical performance, evaluated through crack-onset strain testing, showed that the pristine VO1 film cracked at just ∼20% strain, while blends 75 : 25 and 50 : 50 VO1 : SEBS endured ∼60% and ∼80% strain, respectively. Films with 25 : 75 and 10 : 90 VO1 : SEBS showed no visible cracking even under 100% strain. OFETs built from a 25 : 75 VO1 : SEBS blend maintained functional transfer and output characteristics under 50% uniaxial strain, with mobility remaining within the same order of magnitude and even increasing slightly, likely due to strain-induced reorganization of the semiconducting domains. Together, these findings establish VO1 : SEBS blends as promising materials for mechanically robust, solution-processable semiconducting films. The combination of stable electrical performance and high mechanical strain tolerance, enabled by vertical phase separation and elastic matrix design, offers a powerful strategy for the development of scalable, flexible, and stretchable organic electronics.

Conflicts of interest

There are no conflicts to declare.

Data availability

The data supporting this article have been included as part of the supplementary information (SI). Supplementary information: additional experimental details such as characterization, films morphologies (TGA, DSC, UV-vis, AFM height images, QNM, POM), electrical characteristics of devices (transfer curves, stretched 25 : 75 VO1 : SEBS), tables of films' RMS and XPS etching time. See DOI: https://doi.org/10.1039/d5tc04351d.

Acknowledgements

This work was supported by the Natural Science and Engineering Research Council of Canada (NSERC) and the Fonds de Recherche du Québec: Nature et Technologie (FRQNT) through the joint NOVA program. J. C. thanks the FRQ for a doctoral scholarship. F. G. thanks NSERC for financial support through a Canada Postgraduate Scholarship – Doctoral (PGS-D). S. R.-G. also acknowledges support of the Canada Foundation for Innovation (CFI) and the Ontario Research Fund for infrastructure. A. L. thanks the CFI and the Canada Research Chairs program.

References

1 A. Ashok, J. P. Singh, A. Kumar and N. Bhagat, *Mater. Adv.*, 2025, **6**, 3386–3415.
2 M. El-Tanani, S. M. Satyam, S. A. Rabbani, Y. El-Tanani, A. A. A. Aljabali, I. Al Faouri and A. Rehman, *Pharmaceutics*, 2025, **17**, 1165.
3 L. Roulleau, L. Vauche, D. Marsan, H. Boutry, L. Colas, J. B. Doré, A. Divay and L. Di Cioccio, *Sustainability*, 2025, **17**, 1339.
4 L. M. Gilbertson, L. Pourzahedi, S. Laughton, X. Y. Gao, J. B. Zimmerman, T. L. Theis, P. Westerhoff and G. V. Lowry, *Nat. Nanotechnol.*, 2020, **15**, 801.
5 A. Ioannou, G. Gohari, P. Papaphilippou, S. Panahirad, A. Akbari, M. R. Dadpour, T. Krasia-Christoforou and V. Fotopoulos, *Environ. Exp. Bot.*, 2020, **176**, 104048.
6 X. X. Cheng, Q. R. Xie and Y. Sun, *Front. Bioeng. Biotech.*, 2023, **11**, 77151.
7 K. Sivula and R. van de Krol, *Nat. Rev. Mater.*, 2016, **1**, 15010.
8 P. F. Ding, D. B. Yang, S. C. Yang and Z. Y. Ge, *Chem. Soc. Rev.*, 2024, **53**, 2350–2387.
9 J. Y. Chen, N. Blanc and A. Laventure, *Mater. Adv.*, 2025, **6**, 4804–4816.
10 H. Bronstein, C. B. Nielsen, B. C. Schroeder and I. McCulloch, *Nat. Rev. Chem.*, 2020, **4**, 66–77.
11 D. L. Zhong, C. Wu, Y. W. Jiang, Y. J. Yuan, M. G. Kim, Y. Nishio, C. C. Shih, W. C. Wang, J. C. Lai, X. Z. Ji, T. Z. Gao, Y. X. Wang, C. Y. Xu, Y. Zheng, Z. Yu, H. X. Gong, N. Matsuhisa, C. Z. Zhao, Y. S. Lei, D. Y. Liu, S. Zhang, Y. Ochiai, S. H. Liu, S. Y. Wei, J. B. H. Tok and Z. N. Bao, *Nature*, 2024, **630**, E12–E12.
12 W. C. Wang, S. H. Wang, R. Rastak, Y. Ochiai, S. M. Niu, Y. W. Jiang, P. K. Arunachala, Y. Zheng, J. Xu, N. Matsuhisa,

X. Z. Yan, S. K. Kwon, M. Miyakawa, Z. T. Zhang, R. Ning, A. M. Foudeh, Y. Yun, C. Linder, J. B. H. Tok and Z. N. Bao, *Nat. Electron.*, 2021, **4**, 143–150.
13 G. T. Mason, C. Lisowski, P. Kulatunga, T. C. Gomes, A. Awada, Y. X. Hsu, Y. C. Chiu and S. Rondeau-Gagné, *Mater. Adv.*, 2025, **6**, 6130–6139.
14 B. Nketia-Yawson, J. H. Lee and J. W. Jo, *Appl. Phys. Lett.*, 2021, **119**, 042103.
15 S. Fratini, M. Nikolka, A. Salleo, G. Schweicher and H. Sirringhaus, *Nat. Mater.*, 2020, **19**, 491–502.
16 M. Chang, D. Choi and E. Egap, *ACS Appl. Mater. Interfaces*, 2016, **8**, 13484–13491.
17 H. Sirringhaus, *Adv. Mater.*, 2014, **26**, 1319–1335.
18 Y. C. Chiang, H. C. Wu, H. F. Wen, C. C. Hung, C. W. Hong, C. C. Kuo, T. Higashihara and W. C. Chen, *Macromolecules*, 2019, **52**, 4396–4404.
19 B. Y. Lu, H. Yuk, S. T. Lin, N. N. Jian, K. Qu, J. K. Xu and X. H. Zhao, *Nat. Commun.*, 2019, **10**, 1043.
20 P. Kulatunga, A. Pillon, S. P. Mckillop, B. H. Lessard, J. F. Trant and S. Rondeau-Gagné, *ACS Appl. Mater. Interfaces*, 2025, **17**, 32691–32700.
21 Z. H. Wang, Y. Si, C. Y. Zhao, D. Yu, W. Wang and G. Sun, *ACS Appl. Mater. Interfaces*, 2019, **11**, 27200–27209.
22 A. Douaki, M. Ahmed, E. Longo, G. Windisch, R. Riaz, S. Inam, T. N. Tran, E. L. Papadopoulou, A. Athanassiou, E. Boselli, L. Petti and P. Lugli, *Adv. Sci.*, 2025, **12**, 2417539.
23 J. Heikenfeld, A. Jajack, J. Rogers, P. Gutruf, L. Tian, T. Pan, R. Li, M. Khine, J. Kim, J. Wang and J. Kim, *Lab Chip*, 2018, **18**, 217–248.
24 M. Mooney, Y. F. Wang, A. Nyayachavadi, S. Zhang, X. D. Gu and S. Rondeau-Gagné, *ACS Appl. Mater. Interfaces*, 2021, **13**, 25175–25185.
25 W. L. Huang, X. M. Liu, Z. C. Ding, Z. L. Wang, C. H. Xu, R. P. Li, S. M. Wang, Y. Wu, R. Qin, Y. Han, Y. H. Geng, S. F. Liu, Y. C. Han and K. Zhao, *Nano Lett.*, 2023, **24**, 441–449.
26 G. Y. Zhang, M. McBride, N. Persson, S. Lee, T. J. Dunn, M. F. Toney, Z. B. Yuan, Y. H. Kwon, P. H. Chu, B. Risteen and E. Reichmanis, *Chem. Mater.*, 2017, **29**, 7645–7652.
27 E. Song, B. Kang, H. H. Choi, D. H. Sin, H. Lee, W. H. Lee and K. Cho, *Adv. Electron. Mater.*, 2016, **2**, 1500250.
28 D. Choi, H. Kim, N. Persson, P. H. Chu, M. Chang, J. H. Kang, S. Graham and E. Reichmanis, *Chem. Mater.*, 2016, **28**, 1196–1204.
29 J. Xu, S. H. Wang, G. J. N. Wang, C. X. Zhu, S. C. Luo, L. H. Jin, X. D. Gu, S. C. Chen, V. R. Feig, J. W. F. To, S. Rondeau-Gagne, J. Park, B. C. Schroeder, C. Lu, J. Y. Oh, Y. M. Wang, Y. H. Kim, H. Yan, R. Sinclair, D. S. Zhou, G. Xue, B. Murmann, C. Linder, W. Cai, J. B. H. Tok, J. W. Chung and Z. N. Bao, *Science*, 2017, **355**, 59.
30 X. H. Wang, Y. M. Zhu, Z. Liu, Y. Yuan and L. Z. Qiu, *Adv. Electron. Mater.*, 2021, **7**, 2100591.
31 J. N. Zhao, L. Sun, Z. Y. Chu, T. Li, F. P. Zhang, L. B. Li and W. H. Zhang, *AIP Adv.*, 2020, **10**, 035020.
32 X. W. Yin, J. L. Yang and H. B. Wang, *Adv. Funct. Mater.*, 2022, **32**, 2202071.
33 Y. F. Wang, K. L. Chen, N. Prine, S. Rondeau-Gagné, Y. C. Chiu and X. D. Gu, *Adv. Funct. Mater.*, 2023, **33**, 2303031.
34 A. Peña-Alcántara, S. Nikzad, L. Michalek, N. Prine, Y. F. Wang, H. X. Gong, E. Ponte, S. Schneider, Y. L. Wu, S. E. Root, M. Q. He, J. B. H. Tok, X. D. Gu and Z. A. Bao, *Adv. Electron. Mater.*, 2023, **9**, 2201055.
35 S. W. Ren, W. Q. Zhang, Z. E. Wang, A. Yassar, J. Y. Chen, M. F. Zeng and Z. R. Yi, *Molecules*, 2024, **29**, 457.
36 T. Lei, Y. Cao, Y. L. Fan, C. J. Liu, S. C. Yuan and J. Pei, *J. Am. Chem. Soc.*, 2011, **133**, 6099–6101.
37 X. Liu, V. Placide, L. Chu, K. M. Haidaraly, L. S. Vargas, C. Adachi, J. W. Wu, B. Heinrich, E. Lacaze, W. S. Yan, A. D'Aléo and F. Mathevet, *Appl. Surf. Sci.*, 2025, **686**, 162057.
38 N. Hazra, K. Gayen, P. Ghosh, B. Hansda and A. Banerjee, *Langmuir*, 2024, **40**, 9462–9470.
39 S. X. Zhang, Z. Wu, D. Liu, Y. Zhao, S. J. Chen, Y. Wang and Y. Q. Liu, *Sci. China Mater.*, 2025, **68**, 1777–1787.
40 M. Gsänger, D. Bialas, L. Z. Huang, M. Stolte and F. Würthner, *Adv. Mater.*, 2016, **28**, 3615–3645.
41 H. W. Luo, C. M. Yu, Z. T. Liu, G. X. Zhang, H. Geng, Y. P. Yi, K. Broch, Y. Y. Hu, A. Sadhanala, L. Jiang, P. L. Qi, Z. X. Cai, H. Sirringhaus and D. Q. Zhang, *Sci. Adv.*, 2016, **2**, e1600076.
42 N. E. Persson, P. H. Chu, M. McBride, M. Grover and E. Reichmanis, *Acc. Chem. Res.*, 2017, **50**, 932–942.
43 F. Gagnon, V. Tremblay, A. Soldera, M. U. Ocheje, S. Rondeau-Gagné, M. Leclerc and J.-F. Morin, *Mater. Adv.*, 2022, **3**, 599–603.
44 S. J. Yoon, H. Kim, C. K. Jeong and Y. K. Lee, *J. Korean Ceram. Soc.*, 2024, **61**, 429–435.
45 J. M. Zuo, T. Y. Jin, H. X. Li, J. H. Li, X. Y. Liu, X. H. Yu, Y. Han and Y. C. Han, *Adv. Funct. Mater.*, 2025, **35**, 2424785.
46 Y. Ito, A. A. Virkar, S. Mannsfeld, J. H. Oh, M. Toney, J. Locklin and Z. A. Bao, *J. Am. Chem. Soc.*, 2009, **131**, 9396–9404.
47 P. Kulatunga, M. Comí, T. C. Gomes, M. Seifi, R. Majidzadeh, M. Al-Hashimi and S. Rondeau-Gagné, *J. Mater. Chem. C*, 2023, **11**, 14661–14670.
48 P. Kulatunga, N. Yousefi and S. Rondeau-Gagné, *Chemosensors*, 2022, **10**, 201.
49 Y. L. Chen, S. Y. Qu, Q. F. Song, W. Shi, H. Li, Q. Yao and L. D. Chen, *ACS Appl. Mater. Interfaces*, 2021, **13**, 15064–15072.
50 J. J. Kaschuk, Y. Al Haj, J. V. Garcia, A. Kamppinen, O. J. Rojas, T. Abitbol, K. Miettunen and J. Vapaavuori, *Carbohyd Polym.*, 2024, **332**, 121877.
51 S. Killada, A. Nathani, A. Karim and C. S. Sharma, *Nano Express*, 2024, **5**, 045007.
52 S. Z. D. Cheng and A. Keller, *Annu. Rev. Mater. Sci.*, 1998, **28**, 533–562.
53 Y. F. Ding, Y. M. Zhu, H. Wang, Y. F. Wang, X. D. Gu, X. H. Wang and L. Z. Qiu, *Macromolecules*, 2022, **55**, 8577–8589.
54 J. Kim, S. Lee, Y. Lee, T. H. Lee, J. Y. Kim and H. Y. Woo, *Sustainable Energ Fuels*, 2025, **9**, 1993–1997.

55 Z. Peng, K. Xian, Y. Cui, Q. Qi, J. Liu, Y. Xu, Y. Chai, C. Yang, J. Hou, Y. Geng and L. Ye, *Adv. Mater.*, 2021, **33**, 2106732.
56 S. Zhang, M. U. Ocheje, S. C. Luo, D. Ehlenberg, B. Appleby, D. Weller, D. S. Zhou, S. Rondeau-Gagné and X. D. Gu, *Macromol. Rapid Commun.*, 2018, **39**, 1800092.
57 K. Kranthiraja, V. Sethumadhavan, S. Kumagai, Y. N. Xu, A. Erhardt, C. R. McNeill, S. Manzhos, J. Takeya and P. Sonar, *Adv. Electron. Mater.*, 2025, **11**, 2400614.
58 R. Kothandaraman, W. E. He, K. Kranthiraja, S. Manzhos, C. R. Mcneill, Y. Li, Y. N. Xu, K. E. Fairfull-Smith, T. Michinobu and P. Sonar, *Adv. Mater. Technol.*, 2025, **10**, 2401518.
59 Y. Zheng, M. Ashizawa, S. Zhang, J. Kang, S. Nikzad, Z. A. Yu, Y. Ochiai, H. C. Wu, H. Tran, J. W. Mun, Y. Q. Zheng, J. B. H. Tok, X. D. Gu and Z. N. Bao, *Chem. Mater.*, 2020, **32**, 5700–5714.
60 T. Sugihara, T. Ohura, K. Homma and H. H. Igawa, *Br. J. Plast. Surg.*, 1991, **44**, 418–422.
61 Q. Zhou, Z. H. Wang, Y. K. Yan, L. F. Yang, K. Chi, Y. J. Wu, W. H. Li, Z. Y. Yi, Y. Q. Liu and Y. Zhao, *npj Flexible Electron.*, 2023, **7**, 35.